Circularly polarized light irradiated ferromagnetic $MnBi_2Te_4$: A possible ideal Weyl semimetal

Shuai Fan,[1,*] Shengpu Huang,[1,*] Zhuo Chen,[1,*] Fangyang Zhan,[1]
Xian-Yong Ding,[1] Da-Shuai Ma,[1,2,†] and Rui Wang[1,2,‡]

[1]*Institute for Structure and Function, Department of Physics, and Chongqing Key Laboratory for Strongly Coupled Physics, Chongqing University, Chongqing 400044, People's Republic of China*

[2]*Center of Quantum Materials and Devices, Chongqing University, Chongqing 400044, People's Republic of China*

(Received 28 April 2024; revised 12 July 2024; accepted 26 August 2024; published 9 September 2024)

The interaction between light and nontrivial energy band topology allows for the precise manipulation of topological quantum states, which has attracted intensive interest in condensed-matter physics. In this work, using first-principles calculations, we studied the topological transition of ferromagnetic (FM) $MnBi_2Te_4$ upon irradiation with circularly polarized light (CPL). We revealed that the $MnBi_2Te_4$ can be driven from an FM insulator to a Weyl semimetal with a minimum number of Weyl points, i.e., two Weyl points (WPs) in systems without time-reversal symmetry. More importantly, in FM $MnBi_2Te_4$ with an out-of-plane easy magnetization axis, we found that the band dispersion of the WP evolves from type-II to type-III and finally to type-I when the light intensity increases. Moreover, we show that the profile of the characteristic Fermi arc of the Weyl semimetal phase is sensitive to changes in light intensity, which enables efficient manipulation of the Fermi arc length of FM $MnBi_2Te_4$ in experiments. In addition, for FM $MnBi_2Te_4$ with an in-plane easy magnetization axis, the system becomes a type-I Weyl semimetal under CPL irradiation. With controllable band dispersion, the length of the Fermi arc, and a minimum number of WPs, our results indicate that CPL-irradiated FM $MnBi_2Te_4$ is an ideal platform for the study of novel transport phenomena in Weyl semimetals with distinct band dispersion.

DOI: 10.1103/PhysRevB.110.125204

I. INTRODUCTION

Topological semimetals, a class of phases with energy band crossings near the Fermi level, have sparked growing interest due to the extension of topological classification and promising realizations of elementary particles [1–5]. According to band degeneracy, topological semimetals can be distinguished into Dirac semimetals [6–9], Weyl semimetals (WSM) [10–13], nodal-line semimetals [14–16], and beyond [17–21]. Among these topologically nontrivial materials, WSMs exhibit novel transport phenomena and are one of the typical representatives. WSMs are featured by Weyl points (WPs) consisting of energy bands with linear dispersion in momentum space, and fermionic excitation near these WPs is depicted by a two-component Weyl equation [22]. It is realized that WPs could be regarded as sources of quantized Berry flux. Dependent on the source and drain of Berry flux, the charges of the WPs (i.e., chirality) are defined to be $+1$ and -1, respectively. Presently, based on the manifold of the Fermi surface, WSMs can be classified into three types [23,24]. Type-I Weyl semimetal exhibits standard WPs where the Fermi surface shrinks to a point near the band crossing [12]. Type-II Weyl semimetal has a significant tilt behavior and is characterized by the coexistence of electron and hole pockets connected by WPs. Between type-I and type-II Weyl semimetals, there is a critical point featured by the appearance of a flat band along a specific direction in momentum space, termed type-III Weyl semimetal. The Fermi surface of a type-III Weyl semimetal is a single line, which results in highly anisotropic effective masses and a finite density of states [25]. Besides the distinct Fermi surface, it is theoretically predicated that the amplitude of the tilt behavior of WPs also leads to the emergence of intricate transport phenomena, such as modified Klein tunneling and unconventional Landau levels [26–30]. To achieve experimental verification of those abovementioned theoretical predictions and obtain a clearer understanding of the Weyl semimetal phase, it remains an open question how to select a natural material candidate that can achieve a minimum number of WPs whose band dispersion could be designed as desired by experimental means.

Recently, Floquet engineering (i.e., periodic driving of polarized light) has played a vital role in artificial manipulation of topological quantum states, leading to a series of breakthroughs in nonequilibrium phases [31–45]. There are two essential reasons for the feasibility of manipulating topological states through the irradiation of light: (i) the symmetry breaking by incident light, and (ii) the k-dependent vector-potential of light would modify the band structure and lead to possible band inversions. For example, due to the fact that circularly polarized light (CPL) breaks time-reversal symmetry (TRS), it is theoretically predicted and experimentally verified that the irradiation of CPL can introduce a certain Dirac mass term to the Dirac cones of the surface states of topological insulators, thereby resulting in Chern insulators [34,36]. Moreover, CPL has been proposed as an efficient

*These authors contributed equally to this work.
†Contact author: madason.xin@gmail.com
‡Contact author: rcwang@cqu.edu.cn

means to drive nodal line semimetals and Dirac semimetals into Weyl semimetals [46–48]. Novel properties, such as ultrafast photocurrent, have been proposed in light irradiated Weyl semimetal [49,50]. While significant progress has been made in this field, the manipulation of band dispersion in Weyl semimetals via Floquet engineering in natural materials remains largely unexplored.

In this work, utilizing first-principles calculations, we meticulously tracked the band-gap evolution of FM $MnBi_2Te_4$ with out-of-plane and in-plane easy magnetization axes under the irradiation of CPL, respectively. We found that both FM phases of $MnBi_2Te_4$ can be driven from an FM insulator to an ideal Weyl semimetal with the minimum number of WPs (two Weyl points for a system without TRS). For FM $MnBi_2Te_4$ with the out-of-plane easy magnetization axis, we observed that increasing the intensity of CPL induces a sequential transformation in the band dispersion of WPs. Specifically, this progression transitions from a type-II dispersion to a type-III dispersion, culminating in a type-I dispersion. The characteristic Fermi arcs and surface states of the Weyl semimetal phase under distinct light intensities were investigated. We found that the profile of the characteristic Fermi arcs on the (010) surface of FM $MnBi_2Te_4$ irradiated with CPL exhibits sensitivity to variations in light intensity, enabling effective control of the Fermi arc length through the incident light. At the end of this work, we reoriented the magnetic orientation of $MnBi_2Te_4$ to the in-plane axis. We found that, in this case, the system could also transition to a Weyl semimetal with two WPs as the light intensity increases. The WPs found in CPL irradiated FM $MnBi_2Te_4$ with an in-plane easy magnetization axis maintain type-I band dispersion until they are annihilated.

II. COMPUTATIONAL METHODS

First-principles calculations were performed by Vienna *Ab initio* Simulation Package [51,52] in the framework of density functional theory (DFT) [53,54]. The electron-ion interaction was treated by projector-augmented-wave potentials [55]. The generalized gradient approximation (GGA) with the Perdew-Burke-Ernzerhof formalism was employed to describe the exchange-correlation functional [56]. The experimental lattice constants were adopted [57]. The energy cutoff of the plane wave basis was set to 350 eV, and a k-mesh with a $9 \times 9 \times 5$ Monkhorst-Pack grid [58] in momentum space was used to determine the band structure. Spin-orbit coupling effects were taken into account in the self-consistent calculations. To deal with the correlation effects of $3d$ electrons in Mn atoms, we employed the GGA + U method [59]. Referring to previous theoretical work on $MnBi_2Te_4$ [60], $U = 4$ eV was adopted. In the process of structural relaxation, the forces on each atom were relaxed to be less than 0.02 eV/Å. The topological properties were revealed by constructing a Wannier-function-based tight-binding (WFTB) Hamiltonian based on maximally localized Wannier function methods combining DFT calculations [61–63]. According to the fat-band analysis, three p orbitals of Bi and Te atoms and five d orbitals of Mn atoms were selected to initialize the maximally localized Wannier functions (MLWFs). Employing the WFTB Hamiltonian, we derived a time-dependent Hamiltonian through the Peierls substitution. Then, the time-dependent Hamiltonian was obtained as [46,48,64,65],

$$H^{\mathrm{W}}_{mn}(\boldsymbol{k}, t) = \sum_{\boldsymbol{R}} e^{i\left[\boldsymbol{k}+\frac{e}{\hbar}\mathbf{A}(t)\right]\left[\boldsymbol{R}-(\boldsymbol{\tau}_m-\boldsymbol{\tau}_n)\right]} t_{mn}(\boldsymbol{R}-\mathbf{0}). \quad (1)$$

Here, $\boldsymbol{k}$ is the wave vector, $\boldsymbol{R}$ is the Bravais lattice vector, $\boldsymbol{\tau}$ denotes the position of Wannier orbitals at the home site $\mathbf{0}$, $t_{mn}(\boldsymbol{R}-\mathbf{0})$ is the hopping amplitude from the Wannier orbital n at the home site $\mathbf{0}$ to the Wannier orbital m at site $\boldsymbol{R}$, and $\mathbf{A}(t)$ is the external time-dependent circularly polarized light. In this paper, only the high-frequency regime is considered. Then, the coupling between different Floquet bands can be ignored, and the effectively static Hamiltonian reads as follows [46,48,64],

$$H^{\mathrm{eff}}_{mn}(\boldsymbol{k}) = H^{0}_{mn}(\boldsymbol{k}) + \sum_{q\geqslant 1} \frac{\left[H^{-q}_{mn}, H^{+q}_{mn}\right]}{\hbar} + O\left(\frac{1}{\omega^2}\right), \quad (2)$$

where $H^{q}_{mn}(\boldsymbol{k}, \omega)$ is the qth-order time-independent Floquet Hamiltonian, which is generally in infinite-dimensional Hilbert space and expressed as

$$H^{q}_{mn}(\boldsymbol{k}, \omega) = \frac{1}{T}\int_0^T e^{-iq\omega t} H^{\mathrm{W}}_{mn}(\boldsymbol{k}, t)dt, \quad (3)$$

where T and ω are the period and frequency of light, respectively. Generally, the qth order time-independent Floquet Hamiltonian $H^{q}_{mn}(\boldsymbol{k}, \omega)$ is in infinite-dimensional Hilbert space. However, the matrix elements of Eq. (3) decay rapidly with $|q|$ in the high-frequency approximation. Thus, in our calculation, we can use the effectively static Hamiltonian with the proper value of q. Here, all results were calculated with $q = 1$. The results were doubly checked with those obtained by setting $q = 2$. The topological surface states and Fermi arcs were calculated based on $H^{\mathrm{eff}}_{mn}(\boldsymbol{k})$ using the WANNIERTOOLS package [66,67].

III. RESULTS AND DISCUSSION

$MnBi_2Te_4$ belongs to a rhombohedral structure with the space group $R\bar{3}m$ (No. 166) [68]. As depicted in Fig. 1(a), the $MnBi_2Te_4$ single crystal is composed of Te-Bi-Te-Mn-Te-Bi-Te septuple layers stacking along the c axis. Two adjacent septuple layers are coupled to each other via van der Waals forces. The experimental lattice parameters of the unit cell are $|\boldsymbol{a}| = |\boldsymbol{b}| = 4.33$ Å and $|\boldsymbol{c}| = 40.91$ Å. In the calculation of the electronic properties for FM $MnBi_2Te_4$, we select the lattice vectors as $\boldsymbol{a}' = \boldsymbol{a}$, $\boldsymbol{b}' = \boldsymbol{b}$, and $\boldsymbol{c}' = [\boldsymbol{c} - (\boldsymbol{a} + \boldsymbol{b})]/3$. It is reported that, due to the Anderson superexchange, the magnetic ground state of bulk $MnBi_2Te_4$ is an A-type AFM phase with an out-of-plane easy magnetization axis. Although the total energy of the FM phases is approximately 0.046 eV higher than that of the A-type AFM phase, the field-induced FM phase of $MnBi_2Te_4$ is reported to be experimentally achievable [69]. Here, we mainly consider the FM-z phase of $MnBi_2Te_4$ with the out-of-plane easy magnetization axis as shown in Fig. 1(a). We examine the topological evolution of the band structure in the FM phase $MnBi_2Te_4$ under left-handed periodic CPL irradiation. Additionally, other FM phases of $MnBi_2Te_4$, such as the FM-y phase with an in-plane easy magnetization axis aligned along the y axis, and the

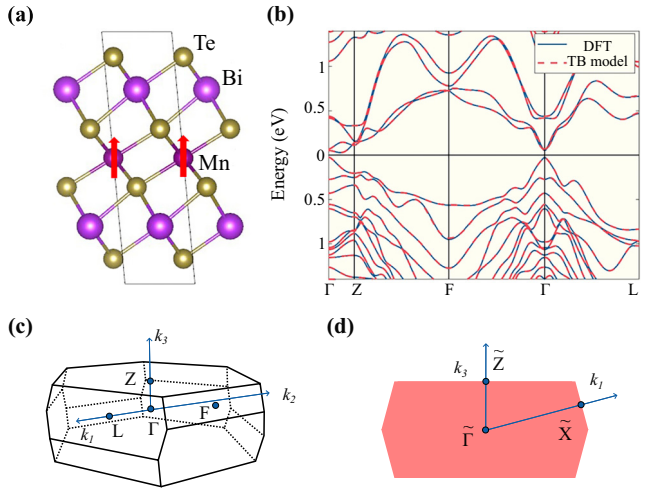

FIG. 1. (a) Crystal and magnetic structures of FM-z $MnBi_2Te_4$. The magnetic moments of the Mn atoms are directed along the red arrows. (b) Electronic structure of FM-z $MnBi_2Te_4$ obtained from DFT calculations (solid blue line) and the Wannier-function-based tight-binding model (dashed red line). (c) Brillouin zone for the conventional cell shown in panel (a) with high-symmetry points marked. (d) Surface BZ for a side surface, i.e., (010) surface.

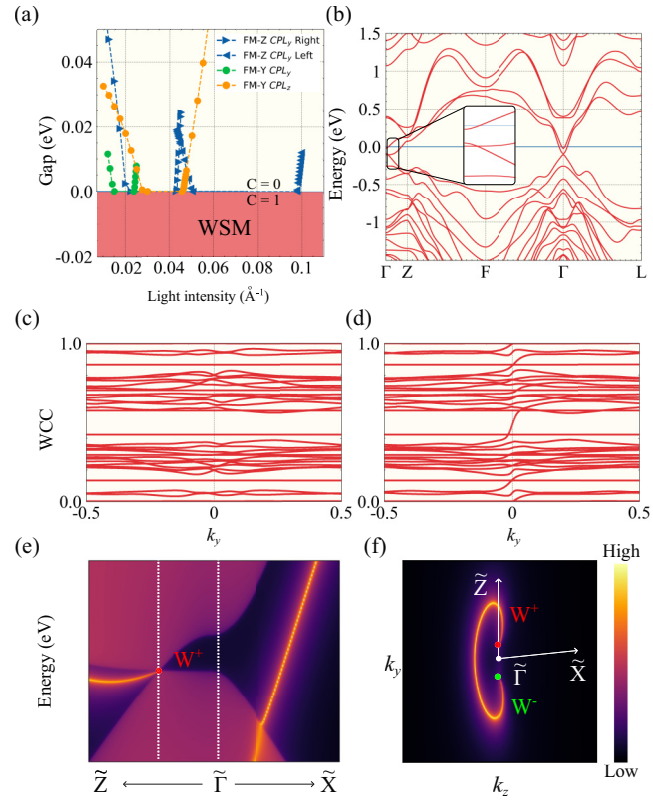

FIG. 2. (a) The evolution of the band gap of FM $MnBi_2Te_4$ with increasing light intensity $eA_1/\hbar$. In this plot, the results for FM-z $MnBi_2Te_4$ irradiated by right- and left-handed CPL with polarization in the x-z plane are marked in blue, while those for FM-y $MnBi_2Te_4$ irradiated by CPL with polarization in the x-z (x-y) plane are marked in green (orange). Moreover, the colors of shaded areas denote different Chern numbers of the $k_3 = 0$ plane. (b) Electronic structure of FM-z $MnBi_2Te_4$ at light intensity $eA_1/\hbar = 0.0300$ Å^{-1}. The inset is the band structure along Γ-Z, where the WP exhibits type-III dispersion. (c) and (d) The Wannier charge centers of FM-z $MnBi_2Te_4$ in the (c) $k_3 = \pi$ plane and (d) the $k_3 = 0$ plane under the irradiation of CPL with light intensity $eA_1/\hbar = 0.0300$ Å^{-1}. (e) The local density of states of the (010) surface of FM-z $MnBi_2Te_4$. (f) The isoenergy band contours of (010) surfaces at -0.104 meV relative to the Fermi level. In panels (e) and (f), the first BZ of the (010) surface is shown in Fig. 1(d), and the projected position of Weyl points with positive and negative chirality are marked in red and blue, respectively.

results obtained by the irradiation of right-handed periodic CPL is briefly discussed at the end of this section.

The bulk Brillouin zone (BZ) of FM-z $MnBi_2Te_4$ is depicted in Fig. 1(b). The band structure of FM-z $MnBi_2Te_4$ along high-symmetry lines within the bulk BZ is shown in Fig. 1(c). It is observed that the system is a FM insulator with an indirect band gap of ∼53 meV. The smallest local band gap, approximately 75 meV, is located at the high-symmetry point Γ. To trace the light-manipulated band topology of FM $MnBi_2Te_4$, we employed the MLWFs to construct a WFTB Hamiltonian from first-principles calculations based on DFT. The band structure of FM-z $MnBi_2Te_4$ obtained from the constructed WFTB Hamiltonian are delineated by the red dashed lines in Fig. 1(c) and is found to be in agreement with results obtained by DFT calculation. Based on this reliable WFTB Hamiltonian, the Peierls substitution is adopted to obtain the time-dependent Hamiltonian, which can capture the electronic properties of FM $MnBi_2Te_4$ when it is irradiated by CPL.

Under irradiation with CPL, the time-dependent vector potential is defined as $\boldsymbol{A}(t) = A_0[\cos(\omega t), 0, \sin(\omega t)]$, where A_0 is the amplitude of the CPL, and ω is the frequency. Hence, the intensity of the light is $eA_0/\hbar$. The incident light irradiates along the y axis and is polarized within the x-z plane. In our calculations, $\hbar\omega = 15$ eV is adopted to avoid interactions between different Floquet sub-bands. As depicted in Fig. 2(a), we show the evolution of the band gap of FM-z $MnBi_2Te_4$ under light irradiation with varying intensities (i.e., $eA_0/\hbar = 0.0100$ Å^{-1} ↦ 0.1000 Å^{-1}). It was found that light irradiation significantly changes the energy band profile as the amplitude increases. When the light intensities exceed $eA_0/\hbar = 0.0200$ Å^{-1}, band crossings occur along the high-symmetry line Γ-Z, indicating the transformation of FM-z $MnBi_2Te_4$ from trivial insulators to semimetals. Meanwhile, FM-z $MnBi_2Te_4$ becomes a trivial insulator again when the intensity of light exceeds $eA_0/\hbar = 0.0430$ Å^{-1}. Notably, this critical value of light intensity corresponds to the electric field strength of 6.459×10^9 V/m or the peak intensity of 5.541×10^{12} W/cm^2. It is reported that the damage threshold is approximately 10^7–10^8 V/m for topological materials Bi_2Se_3 and black phosphorus [31,34], while that for FeSe and graphene could be up to 10^9–10^{10} V/m [70,71]. The value of the electric field of 6.459×10^9 V/m applied to FM-z $MnBi_2Te_4$ is close to the damage threshold of the above-mentioned materials. Since there is no direct experimental evidence for the damage threshold of $MnBi_2Te_4$, the experimental feasibility of our proposal needs to be verified by upcoming experimental work. Through careful searching of local minimum of energy differences between valence and conduction bands, we find that, in the specific range of light

intensity (i.e., 0.0200 Å^{-1} ↦ 0.0430 Å^{-1}), there are only two WPs pinned on the high-symmetry line Γ-Z in the whole bulk BZ.

Let us turn to FM-z $MnBi_2Te_4$ under the irradiation of CPL with a light intensity of $eA_0/\hbar = 0.0300$ Å^{-1} and detect the band topology of the Weyl semimetal phase. In this case, as shown in Fig. 2(b), the two WPs with chirality ±1 are positioned at ±(0.000, 0.000, 0.024) Å^{-1}, located at ∼ − 0.104 eV relative to the Fermi level, and are labeled as $W^{\pm}$. The energy dispersion of FM-z $MnBi_2Te_4$ with $eA_0/\hbar = 0.0300$ Å^{-1} along Γ-Z is inserted in Fig. 2(b). One can observe that the Weyl node W^+, exhibiting type-III dispersion, consists of one flat band and one dispersive band. Due to the remaining inversion symmetry $\mathcal{P}$ under irradiation, the WP W^- keeps the same dispersion with W^+. Furthermore, to illustrate the nontrivial band topology of this Weyl semimetal phase, we present the surface state of FM-z $MnBi_2Te_4$ with $eA_0/\hbar = 0.0300$ Å^{-1} by using the Floquet WFTB Hamiltonian. The obtained local density of states (LDOS) projected on the semi-infinite (010) surface is presented in Fig. 2(e). It is observed that the characteristic topological Fermi arc terminates at the projected WP W^+ and extends along the $\widetilde{\Gamma}$-$\widetilde{Z}$ direction. Moreover, the Fermi arc is found along the $\widetilde{\Gamma}$-$\widetilde{X}$ direction. In order to fully understand the appearance of the Fermi arc, we calculated the evolution of Wannier charge centers [72] in the $k_z = 0$ and π two-dimensional planes, as illustrated in Figs. 2(c) and 2(d), respectively. It is found that there is unavoidable Wilson loop winding in the Wilson loop spectrum of $k_z = 0$ plane, whereas a gap is present in the spectrum of $k_z = \pi$ plane. Correspondingly, we have the Chern number $\mathcal{C} = 1$ on the $k_z = 0$ plane, and $\mathcal{C} = 0$ on the $k_z = \pi$ plane, indicating that, when projected onto a plane perpendicular to the z axis, the Fermi arc will intersect the $k_z = 0$ line of the surface BZ an odd number of times. To confirm this prediction, we further examined isoenergy contours of the semi-infinite (010) surface, as shown in Fig. 2(f). The isoenergy band contours of the (010) surfaces at −0.104 meV relative to the Fermi level are shown in Fig. 2(f), where the projected positions of WPs are marked. Figure 2(f) indicates that there is one Fermi arc connecting the projections of WPs with opposite chirality and intersecting the $k_z = 0$ line once. These two WPs, which are close to the Fermi level, are well separated in momentum space (i.e., 0.0600 Å^{-1}), and the Fermi arcs are clearly discernible, greatly facilitating experimental observation.

This light-induced WSM, with a minimum number of WPs, exhibits remarkable topological features. Due to the momentum-dependent nature of light coupling, the positions and band dispersions of the two WPs will evolve with the light amplitude A_0. In FM-z $MnBi_2Te_4$, the band dispersion of WPs undergoes a light-dependent transition when the intensity $eA_0/\hbar$ increases from 0.020 to 0.043 Å^{-1}. The band dispersions with $eA_0/\hbar = 0.0225$, 0.0300, and 0.0375 Å^{-1} along Γ-Z are illustrated in Figs. 3(a)–3(c), respectively. It is found that the dispersion of WP $W^{\pm}$ transit sequentially from type-II to type-III and finally to type-I. To further substantiate this transition, we obtained the Fermi surface in the $k_2 = 0$ plane of the bulk band structure of FM-z $MnBi_2Te_4$ with $eA_0/\hbar = 0.0225$, 0.0300, and 0.0375 Å^{-1}. With energies corresponding to the respective WPs, the isoenergy contours

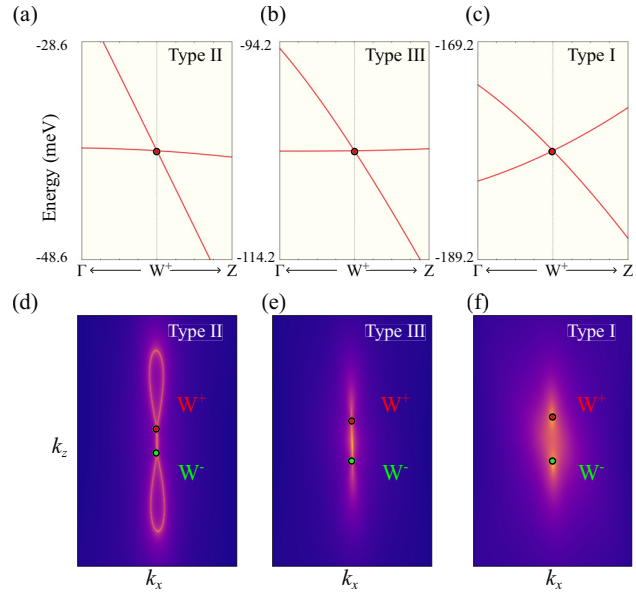

FIG. 3. (a)–(c) Calculated band structure of FM-z $MnBi_2Te_4$ along the high-symmetry line Γ-Z with the light intensity $eA_1/\hbar$ of (a) 0.0225 Å^{-1}, (b) 0.0300 Å^{-1}, and (c) 0.0375 Å^{-1}. (d)–(f) Isoenergy contour in the $k_2 = 0$ plane of the bulk band structure of FM-z $MnBi_2Te_4$ with $eA_1/\hbar$ of (d) 0.0225 Å^{-1}, (e) 0.0300 Å^{-1}, and (f) 0.0375 Å^{-1}. In plots (d)–(f), the energies of the isoenergy contours correspond to those of the respective WPs.

are presented in Figs. 2(d)–2(f). In Fig. 2(d), it is found that when $eA_0/\hbar = 0.0225$ Å^{-1}, the WPs connect the electron and hole pockets, demonstrating type-II dispersion. In contrast, as shown in Fig. 2(f), for $eA_0/\hbar = 0.0375$ Å^{-1}, the isoenergy contour of this system consists of two isolated points, indicating type-I dispersion of WPs.

As the light intensity increases, the characteristic surface states of WPs in the bulk FM-z $MnBi_2Te_4$ undergo significant changes. The calculated LDOSs projected on the semi-infinite (010) surface of FM-z $MnBi_2Te_4$ with a light intensity $eA_0/\hbar$ of 0.0225 and 0.0375 Å^{-1} are respectively shown in Figs. 3(a) and 3(c). It is observed that upon an increase in light intensity, the slope of the surface state near WP decreases and eventually becomes negative. Consequently, in contrast to $eA_0/\hbar = 0.0225$ Å^{-1} [as detailed in Fig. 4(b)], when $eA_0/\hbar = 0.0375$ Å^{-1}, the Fermi arc no longer intersects the high-symmetry line $\widetilde{Z}$-$\widetilde{\Gamma}$ but instead directly links the two WPs, as depicted in Fig. 4(d). Thus, the length of the Fermi arc is acutely sensitive to variations in light intensity, which affords greater flexibility in manipulating the Weyl semimetal phase in CPL irradiated FM-z $MnBi_2Te_4$.

Finally, in addition to FM-z $MnBi_2Te_4$, we have also briefly investigated the band topology of FM-y $MnBi_2Te_4$. We consider two kinds of CPL, i.e., $\boldsymbol{A}_0(t) = A_0[\cos(\omega t), 0, \sin(\omega t)]$ and $\boldsymbol{A}_1(t) = A_1[\cos(\omega t), \sin(\omega t), 0]$. For both cases, we traced the minimal local band gap of FM-y $MnBi_2Te_4$. As shown in Fig. 2(a), FM-y $MnBi_2Te_4$ can be driven to be semimetal under irradiation of $\boldsymbol{A}_0(t)$ or $\boldsymbol{A}_1(t)$. For FM-y $MnBi_2Te_4$ irradiated by $\boldsymbol{A}_1(t)$, when the light intensity $eA_1/\hbar$ is between 0.0300 and 0.0460 Å^{-1}, the materials exhibit a type-I WSM phase with a pair of WPs. Similarly,

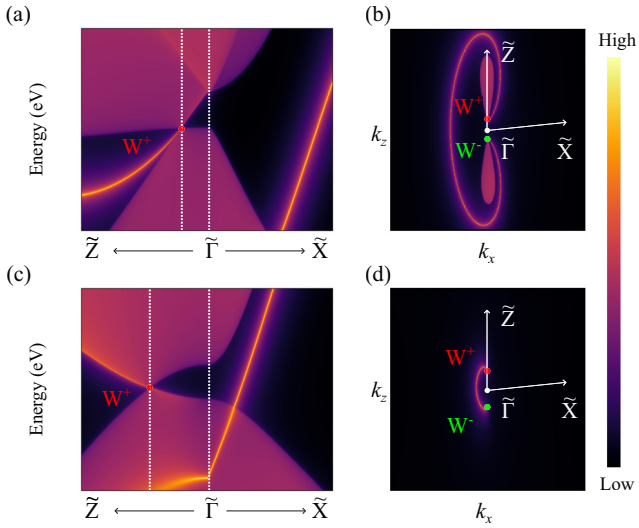

FIG. 4. (a)–(d) Calculated surface states and corresponding Fermi arcs for the (010) surface of FM-z $MnBi_2Te_4$ with irradiation of CPL. In plots (a) and (b), $eA_0/\hbar = 0.0225$ Å^{-1} is adopted, while the light intensity is set as $eA_0/\hbar = 0.0375$ Å^{-1} in plots (c) and (d).

when the light intensity of $eA_0/\hbar$ is between 0.0150 and 0.0240 Å^{-1}, FM-y $MnBi_2Te_4$ is a Weyl semimetal with one pair of type-I WPs. In contrast to FM-z $MnBi_2Te_4$, the light-induced type-I WPs in FM-y $MnBi_2Te_4$ maintain their band dispersion throughout the entire phase diagram. Additionally, as shown in Fig. 2(a), we show the evolution of the band gap of FM-z $MnBi_2Te_4$ irradiation of right-handed CPL that irradiates along the y axis and is polarized within the x-z plane. It is found that the right-handed CPL can also transform FM $MnBi_2Te_4$ from an insulator to a Weyl semimetal.

In the community of condensed-matter physics, the discovery and manipulation of the simplest Weyl semimetal that is experimentally achievable and possesses a single pair of Weyl points is a long-sought goal. Presently, there are a few proposed candidates, such as $HgCr_2Se_4$ [11], strained FM $MnBi_2Te_4$ [60,73,74], and XCrTe (X = K and Rb) [75]. However, due to certain drawbacks, these pioneering candidates face challenges in experimental realization and application. Here, the realization of the simplest Weyl semimetal in FM $MnBi_2Te_4$ under periodic CPL irradiation has some advantages.

(i) Except the WPs, there are no other extraneous bands crossing the Fermi level.

(ii) The band dispersion, the distance between two WPs, and the length of the Fermi arc are all manipulable by the intensities of the light.

(iii) Inspired by a recent experiment where the light-induced anomalous Hall effect in graphene has been observed [36], the light-induced and light-manipulable Weyl semimetal phase would be experimentally achievable.

In conclusion, we theoretically propose that FM $MnBi_2Te_4$ exhibits ideal WSM characteristics with a minimum number of WPs under the irradiation of a CPL. Notably, the WPs are controllable by tuning the amplitude of the incident light. Specifically, for FM $MnBi_2Te_4$ with out-of-plane magnetic orientation, the band dispersion of WPs transitions sequentially from type-II to type-III, and ultimately to type-I, as the light intensity increases. Moreover, we show that the profile of the characteristic Fermi arcs connecting the projections of WPs on the (010) surface of CPL irradiated FM-z $MnBi_2Te_4$ is sensitive to variations in light intensity. Consequently, the length of the Fermi arc can be effectively controlled by the incident light. When the magnetic orientation is rotated to the in-plane axis, the FM-y $MnBi_2Te_4$ can be driven from FM insulator to Weyl semimetal by CPL irradiating along the y or z axis. Different than the case of FM-z $MnBi_2Te_4$ where different types of WPs are found, the WPs found in CPL irradiated FM-y $MnBi_2Te_4$ maintain type-I band dispersion until they are annihilated. Our work shows that irradiation of CPL in FM $MnBi_2Te_4$ is an efficient means to achieve ideal Weyl semimetals with desired dispersion, which will arouse wide concern of design and light-manipulated nontrivial band topology.

ACKNOWLEDGMENTS

This work was supported by the National Natural Science Foundation of China (NSFC, Grants No. 12204074, No. 12222402, No. 11974062, and No. 92365101) and the Natural Science Foundation of Chongqing (Grant No. CSTB2023NSCQJQX0024). D.-S.M. also acknowledges funding from the China National Postdoctoral Program for Innovative Talent (Grant No. BX20220367), and the founding from China Postdoctoral Science Foundation (Grant No. 2023M740411).

[1] M. Z. Hasan and C. L. Kane, *Colloquium*: Topological insulators, Rev. Mod. Phys. **82**, 3045 (2010).

[2] X.-L. Qi and S.-C. Zhang, Topological insulators and superconductors, Rev. Mod. Phys. **83**, 1057 (2011).

[3] N. P. Armitage, E. J. Mele, and A. Vishwanath, Weyl and Dirac semimetals in three-dimensional solids, Rev. Mod. Phys. **90**, 015001 (2018).

[4] H. Gao, J. W. Venderbos, Y. Kim, and A. M. Rappe, Topological semimetals from first principles, Annu. Rev. Mater. Res. **49**, 153 (2019).

[5] A. A. Burkov, Topological semimetals, Nat. Mater. **15**, 1145 (2016).

[6] Z. J. Wang, Y. Sun, X.-Q. Chen, C. Franchini, G. Xu, H. M. Weng, X. Dai, and Z. Fang, Dirac semimetal and topological phase transitions in A_3 Bi (A = Na, K, Rb), Phys. Rev. B **85**, 195320 (2012).

[7] Z. K. Liu, B. Zhou, Y. Zhang, Z. J. Wang, H. M. Weng, D. Prabhakaran, S.-K. Mo, Z. X. Shen, Z. Fang, X. Dai, Z. Hussain, and Y. L. Chen, Discovery of a three-dimensional topological Dirac semimetal, Na_3Bi, Science **343**, 864 (2014).

[8] J. M. Ok, N. Mohanta, J. Zhang, S. Yoon, S. Okamoto, E. S. Choi, H. Zhou, M. Briggeman, P. Irvin, A. R. Lupini, Y.-Y. Pai, E. Skoropata, C. Sohn, H. Li, H. Miao, B. Lawrie, W. S. Choi, G. Eres, J. Levy, and H. N. Lee, Correlated oxide Dirac

semimetal in the extreme quantum limit, Sci. Adv. **7**, eabf9631 (2021).

[9] C. H. Bao, Q. Li, S. Xu, S. H. Zhou, X.-Y. Zeng, H. Y. Zhong, Q. X. Gao, L. P. Luo, D. Sun, T.-L. Xia, and S. Y. Zhou, Population inversion and Dirac fermion cooling in 3D Dirac semimetal Cd_3As_2, Nano Lett. **22**, 1138 (2022).

[10] X. G. Wan, A. M. Turner, A. Vishwanath, and S. Y. Savrasov, Topological semimetal and Fermi-arc surface states in the electronic structure of pyrochlore iridates, Phys. Rev. B **83**, 205101 (2011).

[11] G. Xu, H. M. Weng, Z. J. Wang, X. Dai, and Z. Fang, Chern semimetal and the quantized anomalous Hall effect in $HgCr_2Se_4$, Phys. Rev. Lett. **107**, 186806 (2011).

[12] A. A. Soluyanov, D. Gresch, Z. J. Wang, Q. S. Wu, M. Troyer, X. Dai, and B. A. Bernevig, Type-II Weyl semimetals, Nature (London) **527**, 495 (2015).

[13] S. M. Nie, T. Hashimoto, and F. B. Prinz, Magnetic Weyl semimetal in $K_2Mn_3(AsO_4)_3$ with the minimum number of Weyl points, Phys. Rev. Lett. **128**, 176401 (2022).

[14] A. A. Burkov, M. D. Hook, and L. Balents, Topological nodal semimetals, Phys. Rev. B **84**, 235126 (2011).

[15] Y. Kim, B. J. Wieder, C. L. Kane, and A. M. Rappe, Dirac line nodes in inversion-symmetric crystals, Phys. Rev. Lett. **115**, 036806 (2015).

[16] R.-Y. Liu, A. Huang, R. Sankar, J. A. Hlevyack, C.-C. Su, S.-C. Weng, M.-K. Lin, P. Chen, C.-M. Cheng, J. D. Denlinger, S.-K. Mo, A. V. Fedorov, C.-S. Chang, H.-T. Jeng, T.-M. Chuang, and T.-C. Chiang, Dirac nodal line in hourglass semimetal Nb_3SiTe_6, Nano Lett. **23**, 380 (2023).

[17] Z. M. Zhu, G. W. Winkler, Q. S. Wu, J. Li, and A. A. Soluyanov, Triple point topological metals, Phys. Rev. X **6**, 031003 (2016).

[18] B. Q. Lv, Z.-L. Feng, Q.-N. Xu, X. Gao, J.-Z. Ma, L.-Y. Kong, P. Richard, Y.-B. Huang, V. N. Strocov, C. Fang, H.-M. Weng, Y.-G. Shi, T. Qian, and H. Ding, Observation of three-component fermions in the topological semimetal molybdenum phosphide, Nature (London) **546**, 627 (2017).

[19] B. J. Wieder, Y. Kim, A. M. Rappe, and C. L. Kane, Double Dirac semimetals in three dimensions, Phys. Rev. Lett. **116**, 186402 (2016).

[20] B. Bradlyn, J. Cano, Z. J. Wang, M. G. Vergniory, C. Felser, R. J. Cava, and B. A. Bernevig, Beyond Dirac and Weyl fermions: Unconventional quasiparticles in conventional crystals, Science **353**, aaf5037 (2016).

[21] S.-S. Wang, Y. Liu, Z.-M. Yu, X.-L. Sheng, and S. Y. A. Yang, Hourglass Dirac chain metal in rhenium dioxide, Nat. Commun. **8**, 1844 (2017).

[22] B. H. Yan and C. Felser, Topological materials: Weyl semimetals, Annu. Rev. Condens. Matter Phys. **8**, 337 (2017).

[23] E. J. Bergholtz, Z. Liu, M. Trescher, R. Moessner, and M. Udagawa, Topology and interactions in a frustrated slab: Tuning from Weyl semimetals to $\mathcal{C} > 1$ fractional Chern insulators, Phys. Rev. Lett. **114**, 016806 (2015).

[24] M. Trescher, B. Sbierski, P. W. Brouwer, and E. J. Bergholtz, Quantum transport in Dirac materials: Signatures of tilted and anisotropic Dirac and Weyl cones, Phys. Rev. B **91**, 115135 (2015).

[25] M. Milićević, G. Montambaux, T. Ozawa, O. Jamadi, B. Real, I. Sagnes, A. Lemaître, L. Le Gratiet, A. Harouri, J. Bloch, and A. Amo, Type-III and tilted Dirac cones emerging from flat bands in photonic orbital graphene, Phys. Rev. X **9**, 031010 (2019).

[26] T. E. O'Brien, M. Diez, and C. W. J. Beenakker, Magnetic breakdown and Klein tunneling in a type-II Weyl semimetal, Phys. Rev. Lett. **116**, 236401 (2016).

[27] Z.-M. Yu, Y. G. Yao, and S. Y. A. Yang, Predicted unusual magnetoresponse in type-II Weyl semimetals, Phys. Rev. Lett. **117**, 077202 (2016).

[28] V. H. Nguyen and J.-C. Charlier, Klein tunneling and electron optics in Dirac-Weyl fermion systems with tilted energy dispersion, Phys. Rev. B **97**, 235113 (2018).

[29] X. Yuan, Z. B. Yan, C. Y. Song, M. Y. Zhang, Z. L. Li, C. Zhang, Y. W. Liu, W. Y. Wang, M. H. Zhao, Z. H. Lin, T. Xie, J. Ludwig, Y. X. Jiang, X. X. Zhang, C. Shang, Z. F. Ye, J. X. Wang, F. Chen, Z. C. Xia, D. Smirnov *et al.*, Chiral Landau levels in Weyl semimetal NbAs with multiple topological carriers, Nat. Commun. **9**, 1854 (2018).

[30] P. Liu, C. X. Cui, X.-P. Li, Z.-M. Yu, and Y. G. Yao, Landau level spectrum and magneto-optical conductivity in tilted Weyl semimetal, Phys. Rev. B **107**, 085146 (2023).

[31] H. Liu, J.-T. Sun, C. Cheng, F. Liu, and S. Meng, Photoinduced nonequilibrium topological states in strained black phosphorus, Phys. Rev. Lett. **120**, 237403 (2018).

[32] N. H. Lindner, G. Refael, and V. Galitski, Floquet topological insulator in semiconductor quantum wells, Nat. Phys. **7**, 490 (2011).

[33] T. Kitagawa, T. Oka, A. Brataas, L. Fu, and E. Demler, Transport properties of nonequilibrium systems under the application of light: Photoinduced quantum Hall insulators without Landau levels, Phys. Rev. B **84**, 235108 (2011).

[34] Y. H. Wang, H. Steinberg, P. Jarillo-Herrero, and N. Gedik, Observation of Floquet-Bloch states on the surface of a topological insulator, Science **342**, 453 (2013).

[35] R. Chen, D.-H. Xu, and B. Zhou, Floquet topological insulator phase in a Weyl semimetal thin film with disorder, Phys. Rev. B **98**, 235159 (2018).

[36] J. W. McIver, B. Schulte, F.-U. Stein, T. Matsuyama, G. Jotzu, G. Meier, and A. Cavalleri, Light-induced anomalous Hall effect in graphene, Nat. Phys. **16**, 38 (2020).

[37] F. Mahmood, C.-K. Chan, Z. Alpichshev, D. Gardner, Y. Lee, P. A. Lee, and N. Gedik, Selective scattering between Floquet-Bloch and Volkov states in a topological insulator, Nat. Phys. **12**, 306 (2016).

[38] C. H. Bao, P. Z. Tang, D. Sun, and S. Y. Zhou, Light-induced emergent phenomena in 2D materials and topological materials, Nat. Rev. Phys. **4**, 33 (2022).

[39] F. Y. Zhan, J. J. Zeng, Z. Chen, X. Jin, J. Fan, T. Y. Chen, and R. Wang, Floquet engineering of nonequilibrium valley-polarized quantum anomalous Hall effect with tunable Chern number, Nano Lett. **23**, 2166 (2023).

[40] Z.-M. Wang, R. Wang, J.-H. Sun, T.-Y. Chen, and D.-H. Xu, Floquet Weyl semimetal phases in light-irradiated higher-order topological Dirac semimetals, Phys. Rev. B **107**, L121407 (2023).

[41] G. Usaj, P. M. Perez-Piskunow, L. E. F. Foa Torres, and C. A. Balseiro, Irradiated graphene as a tunable Floquet topological insulator, Phys. Rev. B **90**, 115423 (2014).

[42] T. Oka and H. Aoki, Photovoltaic Hall effect in graphene, Phys. Rev. B **79**, 081406(R) (2009).

[43] M. Ezawa, Photoinduced topological phase transition and a single Dirac-cone state in silicene, Phys. Rev. Lett. **110**, 026603 (2013).

[44] T. Oka and S. Kitamura, Floquet engineering of quantum materials, Annu. Rev. Condens. Matter Phys. **10**, 387 (2019).

[45] M. S. Rudner and N. H. Lindner, Band structure engineering and non-equilibrium dynamics in Floquet topological insulators, Nat. Rev. Phys. **2**, 229 (2020).

[46] Z. Yan and Z. Wang, Tunable Weyl points in periodically driven nodal line semimetals, Phys. Rev. Lett. **117**, 087402 (2016).

[47] X.-L. Du, R. Chen, R. Wang, and D.-H. Xu, Weyl nodes with higher-order topology in an optically driven nodal-line semimetal, Phys. Rev. B **105**, L081102 (2022).

[48] R. Ji, X. Ding, F. Zhan, X. Xiao, J. Fan, Z. Ning, and R. Wang, Controllable Weyl nodes and Fermi arcs in a light-irradiated carbon allotrope, Phys. Rev. B **108**, 205139 (2023).

[49] A. Bharti and G. Dixit, Tailoring photocurrent in Weyl semimetals via intense laser irradiation, Phys. Rev. B **108**, L161113 (2023).

[50] A. Bharti and G. Dixit, Photocurrent generation in solids via linearly polarized laser, Phys. Rev. B **109**, 104309 (2024).

[51] G. Kresse and J. Furthmüller, Efficient iterative schemes for *ab initio* total-energy calculations using a plane-wave basis set, Phys. Rev. B **54**, 11169 (1996).

[52] G. Kresse and J. Furthmüller, Efficiency of *ab-initio* total energy calculations for metals and semiconductors using a plane-wave basis set, Comput. Mater. Sci. **6**, 15 (1996).

[53] P. Hohenberg and W. Kohn, Inhomogeneous electron gas, Phys. Rev. **136**, B864 (1964).

[54] W. Kohn and L. J. Sham, Self-consistent equations including exchange and correlation effects, Phys. Rev. **140**, A1133 (1965).

[55] P. E. Blöchl, Projector augmented-wave method, Phys. Rev. B **50**, 17953 (1994).

[56] J. P. Perdew, K. Burke, and M. Ernzerhof, Generalized gradient approximation made simple, Phys. Rev. Lett. **77**, 3865 (1996).

[57] M. M. Otrokov, I. I. Klimovskikh, H. Bentmann, D. Estyunin, A. Zeugner, Z. S. Aliev, S. Gaß, A. Wolter, A. Koroleva, A. M. Shikin *et al.*, Prediction and observation of an antiferromagnetic topological insulator, Nature (London) **576**, 416 (2019).

[58] H. J. Monkhorst and J. D. Pack, Special points for Brillouin-zone integrations, Phys. Rev. B **13**, 5188 (1976).

[59] A. I. Liechtenstein, V. I. Anisimov, and J. Zaanen, Density-functional theory and strong interactions: Orbital ordering in Mott-Hubbard insulators, Phys. Rev. B **52**, R5467 (1995).

[60] J. H. Li, Y. Li, S. Q. Du, Z. Wang, B.-L. Gu, S.-C. Zhang, K. He, W. H. Duan, and Y. Xu, Intrinsic magnetic topological insulators in van der Waals layered $MnBi_2Te_4$-family materials, Sci. Adv. **5**, eaaw5685 (2019).

[61] N. Marzari and D. Vanderbilt, Maximally localized generalized Wannier functions for composite energy bands, Phys. Rev. B **56**, 12847 (1997).

[62] A. A. Mostofi, J. R. Yates, Y.-S. Lee, I. Souza, D. Vanderbilt, and N. Marzari, WANNIER90: A tool for obtaining maximally-localised Wannier functions, Comput. Phys. Commun. **178**, 685 (2008).

[63] J. F. Qiao, J. Q. Zhou, Z. Yuan, and W. S. Zhao, Calculation of intrinsic spin Hall conductivity by Wannier interpolation, Phys. Rev. B **98**, 214402 (2018).

[64] N. Goldman and J. Dalibard, Periodically driven quantum systems: Effective Hamiltonians and engineered gauge fields, Phys. Rev. X **4**, 031027 (2014).

[65] U. Bajpai, M. J. H. Ku, and B. K. Nikolić, Robustness of quantized transport through edge states of finite length: Imaging current density in Floquet topological versus quantum spin and anomalous Hall insulators, Phys. Rev. Res. **2**, 033438 (2020).

[66] Q. S. Wu, S. N. Zhang, H.-F. Song, M. Troyer, and A. A. Soluyanov, WANNIERTOOLS: An open-source software package for novel topological materials, Comput. Phys. Commun. **224**, 405 (2018).

[67] M. P. L. Sancho, J. M. Lopez Sancho, J. M. L. Sancho, and J. Rubio, Highly convergent schemes for the calculation of bulk and surface Green functions, J. Phys. F: Met. Phys. **15**, 851 (1985).

[68] D. S. Lee, T.-H. Kim, C.-H. Park, C.-Y. Chung, Y. S. Lim, W.-S. Seo, and H.-H. Park, Crystal structure, properties and nanostructuring of a new layered chalcogenide semiconductor, Bi_2MnTe_4, CrystEngComm **15**, 5532 (2013).

[69] Y. J. Deng, Y. J. Yu, M. Z. Shi, Z. X. Guo, Z. H. Xu, J. Wang, X. H. Chen, and Y. B. Zhang, Quantum anomalous Hall effect in intrinsic magnetic topological insulator $MnBi_2Te_4$, Science **367**, 895 (2020).

[70] M. Sentef, M. Claassen, A. Kemper, B. Moritz, T. Oka, J. Freericks, and T. Devereaux, Theory of Floquet band formation and local pseudospin textures in pump-probe photoemission of graphene, Nat. Commun. **6**, 7047 (2015).

[71] Z. F. Wang, Z. Liu, J. L. Yang, and F. Liu, Light-induced type-II band inversion and quantum anomalous Hall state in monolayer FeSe, Phys. Rev. Lett. **120**, 156406 (2018).

[72] R. Yu, X. L. Qi, A. Bernevig, Z. Fang, and X. Dai, Equivalent expression of $\mathbb{Z}_2$ topological invariant for band insulators using the non-Abelian Berry connection, Phys. Rev. B **84**, 075119 (2011).

[73] D. Q. Zhang, M. J. Shi, T. S. Zhu, D. Y. Xing, H. J. Zhang, and J. Wang, Topological axion states in the magnetic insulator $MnBi_2Te_4$ with the quantized magnetoelectric effect, Phys. Rev. Lett. **122**, 206401 (2019).

[74] P. Li, J. Y. Yu, Y. Wang, and W. D. Luo, Electronic structure and topological phases of the magnetic layered materials $MnBi_2Te_4$, $MnBi_2Se_4$, and $MnSb_2Te_4$, Phys. Rev. B **103**, 155118 (2021).

[75] H. S. Liu, J. Cao, Z. Y. Zhang, J. S. Liang, L. Y. Wang, and S. Y. A. Yang, Ideal spin-polarized Weyl-half-semimetal with a single pair of Weyl points in half-Heusler compounds XCrTe (X = K, Rb), Phys. Rev. B **109**, 174426 (2024).